ACS PHYSICAL CHEMISTRY Au
AN OPEN ACCESS JOURNAL OF THE AMERICAN CHEMICAL SOCIETY

pubs.acs.org/physchemau
Article

Double-Layer Distribution of Hydronium and Hydroxide Ions in the Air−Water Interface

Pengchao Zhang, Muye Feng, and Xuefei Xu*

Cite This: ACS Phys. Chem Au 2024, 4, 336−346
Read Online
ACCESS | Metrics & More | Article Recommendations | Supporting Information

ABSTRACT: The acid−base nature of the aqueous interface has long been controversial. Most macroscopic experiments suggest that the air−water interface is basic based on the detection of negative charges at the interface that indicates the enrichment of hydroxides (OH^-), whereas microscopic studies mostly support the acidic air−water interface with the observation of hydronium (H_3O^+) accumulation in the top layer of the interface. It is crucial to clarify the interfacial preference of OH^- and H_3O^+ ions for rationalizing the debate. In this work, we perform deep potential molecular dynamics simulations to investigate the preferential distribution of OH^- and H_3O^+ ions at the aqueous interfaces. The neural network potential energy surface is trained based on density functional theory calculations with the SCAN functional, which can accurately describe the diffusion of these two ions both in the interface and in the bulk water. In contrast to the previously reported single ion enrichment, we show that both OH^- and H_3O^+ surprisingly prefer to accumulate in interfaces but at different interfacial depths, rendering a double-layer ionic distribution within ∼1 nm near the Gibbs dividing surface. The H_3O^+ preferentially resides in the topmost layer of the interface, but the OH^-, which is enriched in the deeper interfacial layer, has a higher equilibrium concentration due to the more negative free energy of interfacial stabilization [−0.90 (OH^-) vs −0.56 (H_3O^+) kcal/mol]. The present finding of the ionic double-layer distribution may qualitatively offer a self-consistent explanation for the long-term controversy about the acid−base nature of the air−water interface.

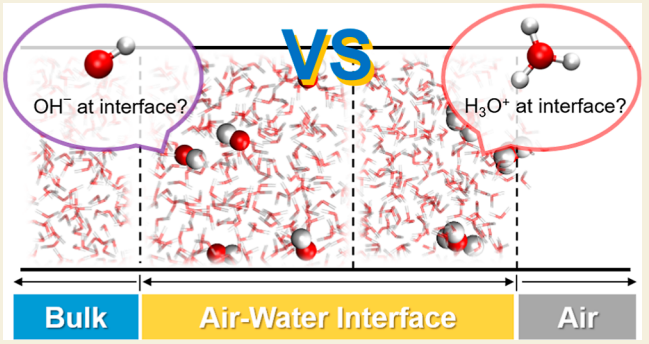

KEYWORDS: *double-layer distribution, air−water interface, hydronium, hydroxide, deep potential, molecular dynamics*

1. INTRODUCTION

Aqueous interfaces are ubiquitous in nature and in engineering applications.[1−4] The acid−base chemistry of aqueous interfaces is critical in fields as diverse as biology, atmospheric science, geochemistry, and engineering.[1,5,6] The accumulated water self-ions at aqueous interfaces, hydroxide OH^- and hydronium H_3O^+, may not only influence the interfacial reactions by changing electrostatic field,[6−9] such as oxygen reduction reaction,[10] hydrogen evolution reaction,[9,11] as well as the formation reactions of hydrogen peroxide,[12−14] ammonia,[15,16] sulfate[17] and phenol,[18] but also directly participate in interfacial physical and chemical processes.[9−14,19,20] Great efforts have been devoted to exploring the preference of water self-ions in the interfaces, as well as their electronic and geometrical structures and dynamic properties for the deep understanding of interfacial acid−base chemistry.[21−45] However, the acid−base chemical characteristics near the interfaces are still elusive,[1,4,46−50] and even whether excess hydroxides and/or hydroniums accumulate in the air−water interface remains controversial.[30−32,36−45]

There has been extensive research into how water self-ions are attracted and distributed in the air−water interfaces.[30,37] The majority of macroscopic experiments indirectly determined the enrichment of OH^- ions and accordingly regarded the aqueous interfaces as basic.[32] In 1861, the first electrophoretic test revealed that air bubbles in the water had a negative zeta potential.[21] Subsequently, it was extensively reported that O_2/N_2/air bubbles[22,29,33] and oil droplets[24,25,33] in water all exhibited the negative zeta potential. It was inferred that the measured negative zeta potential was caused by the interfacial enrichment of OH^- because it is the only anionic source in neat water. In fact, the negative zeta potentials of bubbles and oil droplets were observed even under acidic conditions.[24,26,33] Microscopic experiments, such as second harmonic generation (SHG)[27,30,40] and sum frequency generation (SFG)[30,44,51] spectroscopies, can characterize various interfaces with atomic resolution and have been

Received: December 28, 2023
Revised: April 4, 2024
Accepted: April 5, 2024
Published: April 20, 2024

applied to liquid/liquid interfaces, solid/liquid interfaces, air/water interfaces with surfactant layers, and so forth. A spectroscopic study with the SHG technique provided evidence of OH^- adsorption at the hexadecane/water interface.[40] However, more surface-sensitive spectroscopic measurements found an enhancement of hydronium ions at aqueous interfaces, indicating the acidity of the interfaces.[27,30,44,52]

On the other hand, the majority of microscopic simulations supported the acidic aqueous interfaces.[31] Most molecular dynamics (MD) simulations [including *ab initio* MD (AIMD) with Car−Parrinello[34] and Born−Oppenheimer[31] methods, and classical MD with thermodynamically consistent,[43] reactive,[41] and polarizable[38] force fields] of the water droplet and/or slab found that the H_3O^+ ions tended to accumulate at the topmost layer of the interfaces, and the OH^- ions were repelled into the aqueous bulk.[38,41] The adsorption tendencies of H_3O^+ at interfaces were explained by the dipole orientation in the interfacial electric field[43] and a favorable enthalpic contribution,[41] and the repulsion propensities of OH^- at interfaces were interpreted as results of an enthalpic penalty[41] and a lower entropy.[38] A few computational simulations (which include both AIMD[35,39] and MD with a reactive and polarizable force field[42]) obtained the opposite results; i.e., OH^- rather than H_3O^+ was observed to be slightly accumulated at the air−water interface.[35,39,42] The discrepancy between the simulation results may be due not only to the use of different simulation models and methods but also to the limited simulation scales in space and time.

Given the inconsistency of various measurements and simulations, a trade-off hypothesis that the aqueous interface is neutral at pH = ∼3−4 (pK_w = ∼6−8, rather than ∼14 in the bulk water) was proposed;[30,36,45] i.e., the aqueous interface is both acidic and basic.[30] Nevertheless, to the best of our knowledge, this hypothesis has not been confirmed by either experiments or theoretical simulations.

It is worth pondering why these previous investigations gave conflicting results regarding the preference of water self-ions at aqueous interfaces. From the experimental aspect, there are two possible reasons: (1) detection depths at the aqueous interface using various techniques need to be further clarified,[37] which may have visited different microscale regions of the interface. In particular, the detection depth of SFG spectroscopy is usually at the nanoscale,[53−55] while the definition of interfacial depth in macro-experiments such as zeta potential is ambiguous; (2) more advanced experimental techniques on the atomic scale are yet to be developed. Most experiments aimed at identifying the acid−base nature of interfaces rely on indirect measurements.[22−25,28,29,33] Although the OH dynamics of water molecules at the first interfacial hydration layer can be observed by vibrational SFG spectroscopy,[56−60] which helped to probe the interfacial protons of a 1 M HCl solution,[44] the in-operando detection of ionic distribution along the interfacial depth of the neutral water system with the standard surface-science methods is still challenging.[61−64] By combining with simulation technologies, deeper atomic-scale perspectives can be achieved. In terms of theoretical computations, the modeling scale of accurate AIMD, which is usually limited to simulations for hundreds of water molecules and hundreds of picoseconds due to the expensive computational cost, is far from the actual interface scale and dynamic time scale, so it is possible that these simulation results were slightly deviated. Although classical MD can be applied to larger interfacial systems (including more than thousands of water molecules) for simulations at the nanosecond level, it is almost impossible to accurately describe the diffusion process of self-ions in water with most nonreactive force fields because the reactive process of proton hopping in the Grotthuss mechanism[65,66] is expected to play an important role in the diffusion, which involves the formation and breakage of oxygen−hydrogen bonds and needs to be described with *ab initio* methods or advanced reactive/polarizable force fields.

To improve the microscopic understanding of the acid−base feature at aqueous interfaces from a computational perspective, a possible way is to combine the advantages of classical MD (fast computational speed) and AIMD [high accuracy of the potential energy surface (PES)]. In recent years, deep learning has become an effective method for approximating high-dimensional functions and has offered the possibility of fitting extremely sophisticated PESs. Since Blank et al. pioneered the neural network approach to describe potential energy surfaces,[67] many neural network-based PES fitting methods were subsequently introduced, including the high-dimensional neural network potential (HDNNP),[68] deep potential (DP),[69,70] SchNet,[71] etc., which greatly improved the accuracy and efficiency of MD simulations. Today, large-scale MD based on DP models (DPMD) has been successfully applied in a wide variety of studies involving interfacial[72−74] and many other materials science topics,[75] which is able to achieve *ab initio* levels of accuracy and linear scaling with the number of atoms. Therefore, we are motivated to re-examine the distribution and diffusion of water self-ions at nanoscale interfaces using the DPMD method.

DP models for water systems have been well developed and applied for studying water properties, such as ice nucleation,[76] phase diagrams,[77] and nuclear quantum effects (NQEs).[78,79] In the present work, we trained a DP model capable of accurately describing the water self-ion diffusion and the hydrogen bond (HB) network in both the interface and the bulk water, based on density functional theory (DFT) calculations. Then we performed DPMD simulations for the water slab and droplet systems to investigate the distributions of OH^- and H_3O^+ in the interfaces and the bulk water. Unexpectedly, we observed preferential accumulations of OH^- and H_3O^+ at different depths of the interface. By analyzing the diffusion processes, the distribution frequency profiles of charges, the zeta potential, the free energy, the solvated ion structures, and the HB network of the self-ions, this work may qualitatively provide a mutually self-consistent explanation for the long-standing controversy on the air−water interfacial acid−base nature.

2. METHODS

2.1. Deep Potential Model

The DP model was trained with the DeePMD-kit package,[69,70] based on the reference energy and force calculated by the strongly constrained and appropriately normed (SCAN) meta-generalized-gradient-approximation (meta-GGA) functional.[80] The SCAN functional was chosen because it has been demonstrated to be able to well describe the electrical, structural, and dynamic properties of water molecules and water self-ions in previous tests.[76−78,81−83]

To simulate the diffusion and population of water self-ions both in the bulk water and the air−water interface, the training data set consists of a diverse set of configurations selected from bulk water and interface water, with or without having self-ions. In detail, these data

https://doi.org/10.1021/acsphyschemau.3c00076
ACS Phys. Chem Au 2024, 4, 336−346

sets were generated by the concurrent learning scheme with DP Generator (DP-GEN),[84] which iteratively performs three steps, namely, DP training by the DeePMD-kit,[69,70] DPMD exploration by the LAMMPS,[85] and SCAN labeling by the VASP.[86,87] The initial training data sets used to start the DP-GEN workflows were taken from short-time AIMD trajectory simulations. In the DPMD exploration step, to fully sample the conformational space, various DPMD simulations [e.g., in canonical (*NVT*) and isothermal–isobaric (*NPT*) ensembles, for selected temperatures from 270 to 600 K and selected pressures from 0.2 to 10 bar] were carried out by using the DP models trained in the previous loop. In the SCAN labeling step, the candidate configurations were chosen based on the maximal deviation of forces, which will be added to the current training data set for the next loop.

After iterative training with DP-GEN, in total, 10,914 and 7344 frame configurations were collected for pure water and self-ions containing water systems, respectively. To be able to learn the features of the incomplete HB network near the air–water interface, 400 additional frame configurations of the water slab systems from the AIMD trajectory are added to the final training data set. The details of these data sets are given in Table S3 (Supporting Information). The final DP model gradually converges after 10 million steps with the learning rate from 1×10^{-3} to 1×10^{-8}. The trained DP model was validated for a variety of test data sets with configurations also collected from short-time AIMD trajectories, which were completely independent of the training data sets.

2.2. DPMD Simulations

With the final DP model, the diffusion processes and the interfacial preference of self-ions in water droplet and slab systems were investigated by using the DPMD method. Table 1 provides an overview of the configurational details of these simulation systems, and Figure 1 displays their schematic diagrams. In the droplet systems, a water droplet with a diameter of 50 Å is placed in a periodic cube box with a side length of 80 Å, where the vacuum region is big enough to avoid the influence of periodic boundary conditions. Considering the existence of curvature at the droplet interface, larger and more generalized slab systems were constructed for comparison. In the slab systems, the thicknesses of the water and vacuum layers are set to be 100 and 200 Å, respectively, which are adequate to create the nanoscale air–water interface.

Table 1. Details of DPMD Simulation Systems

system	box size (Å^3)	no. of H_2O	no. (molarity) of H_3O^+	no. (molarity) of OH^-
droplet 1	80 × 80 × 80	2267	0	0
droplet 2	80 × 80 × 80	2257	0	10 (0.25 M)
droplet 3	80 × 80 × 80	2257	10 (0.25 M)	0
slab 1	41 × 41 × 300	5500	0	0
slab 2	41 × 41 × 300	5476	0	24 (0.24 M)
slab 3	41 × 41 × 300	5476	24 (0.24 M)	0
slab 4	41 × 41 × 300	5460	20 (0.20 M)	20 (0.20 M)

All of the DPMD simulations were performed at 300 K in the *NVT* ensemble using the LAMMPS package,[85] and some slab systems were also simulated at 275, 330, and 370 K to analyze temperature effects and mimic the nuclear quantum effects (NQEs). (NQEs were expected to accelerate the diffusion of water self-ions due to the quantum delocalization of protons[88]). The temperatures were conserved with the Nosé–Hoover thermostat[89,90] using a damping time of 0.1 ps. In the initial state, the self-ions were randomly placed in all of the simulation systems. All trajectories were simulated for 30 ns with a time step of 1 fs. The diffusions of water self-ions reached the dynamic equilibrium within the first 10 ns of the simulation, so the analysis was carried out based on the data of the last 20 ns with intervals of 1 ps for droplet systems and 4 ps for slab systems, respectively. The visualization of the simulation results was generated by VMD[91] and Matplotlib.[92] Postprocessing of HB analysis was conducted using the MDAnalysis package.[93]

3. RESULTS AND DISCUSSION

3.1. Validation of the DP Model

3.1.1. Comparison with the SCAN Calculations. We first examined the validity of the trained DP model for the test data set. Compared to the SCAN results (Figure S2 in the Supporting Information), the deviation of the DP model is typically less than 1.50 meV/atom in the absolute energy and less than 0.10 eV/Å in the atomic force. Specifically, the root-mean-square errors (RMSEs) of energy and force are 0.67 meV/atom and 0.035 eV/Å for the pure water system and 1.46 meV/atom and 0.038 eV/Å for the self-ion containing system, respectively. The high accuracy achieved on the test data set indicates the adequacy of configurational sampling.

3.1.2. Performance in the Prediction of Structures and Dynamic Properties. We further tested the performance of the DP model in predicting the water structure and the dynamic properties of water self-ions. The radial distribution functions (RDFs) of the pure water system obtained from DPMD simulation were compared with those from AIMD. As

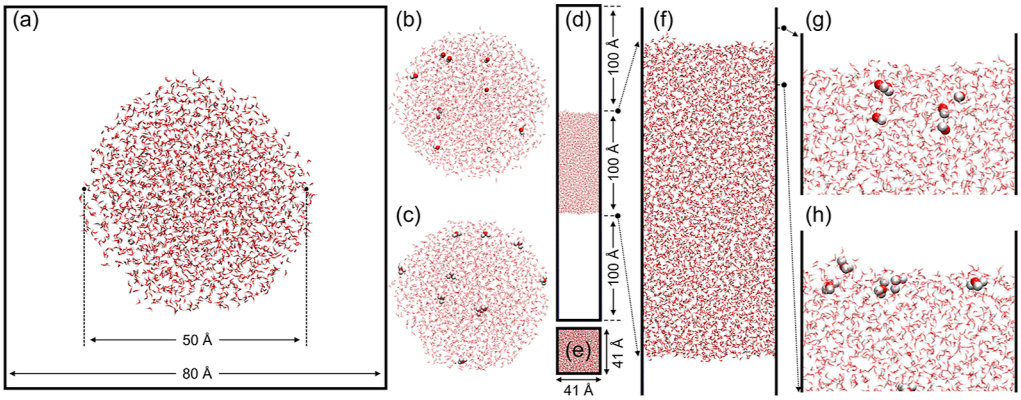

Figure 1. Schematic diagrams of droplet and slab systems. (a) Droplet 1: a pure water droplet located at the center of the periodic box; (b) droplet 2: a hydroxide-containing water droplet; (c) droplet 3: a hydronium-containing water droplet; (d) side view of slab systems; (e) top view of slab systems; (f) zoom-in side view of slab systems; (g) hydroxides in the air–water interface of the slab 2 system; (h) hydroniums in the air–water interface of the slab 3 system. The water self-ions are represented by the ball model, and the water molecules are represented by the stick model. The red and white colors represent the oxygen and hydrogen atoms, respectively.

https://doi.org/10.1021/acsphyschemau.3c00076
ACS Phys. Chem Au 2024, 4, 336–346

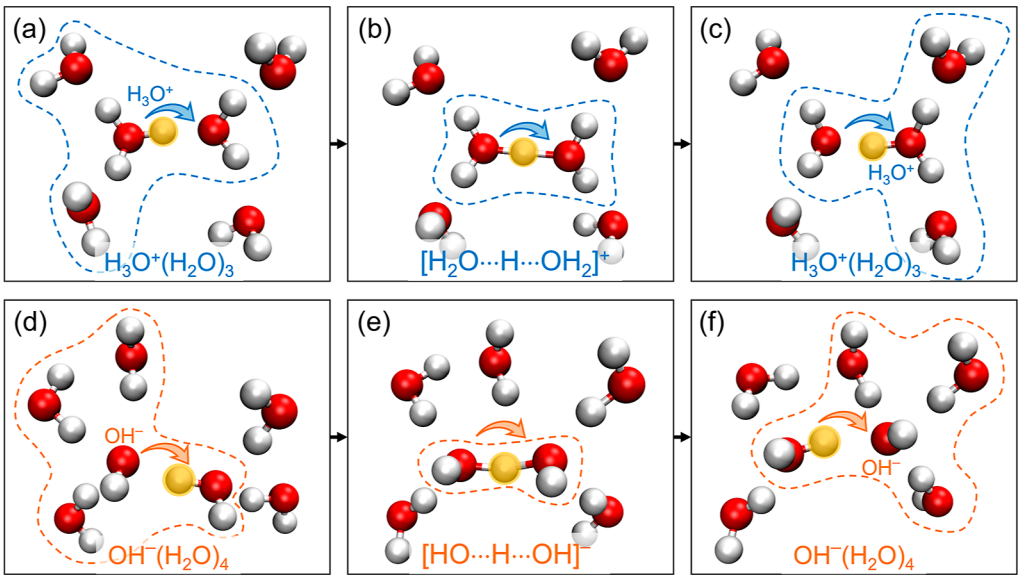

Figure 2. Schematic diagrams of hydronium and hydroxide diffusion. (a–c) Hydronium and (d–f) hydroxide diffusion processes are extracted from the DPMD simulations of slab systems. The transferring protons are shaded in yellow, and the direction of self-ion diffusion is marked by arrows. Surrounding water molecules beyond the first-solvation shell are hidden.

shown in Figure S4, the RDF curves of DPMD and AIMD agree very well, reflecting the accuracy of the DP model in describing the water structure.

The dynamic self-ion diffusion process in water has been extensively studied theoretically[65,94,95] and experimentally.[96] It is widely accepted that the proton diffusion in water follows the Grotthuss mechanism,[66] in which the proton forms water wires with neighboring water molecules, and the H_3O^+ diffusion is achieved by rapid transitions between Eigen and Zundel configurations. Our DPMD simulations also observed the proton diffusion path following the Grotthuss mechanism. As shown in Figure 2a–c, the structural diffusion process of H_3O^+ is achieved by the interconversion of two Eigen configurations ($H_3O^+(H_2O)_3$) via an intermediate Zundel configuration ($[H_2O\cdots H\cdots OH_2]^+$). We discovered the OH^- diffusion processes with the help of proton hopping in our DPMD simulations, as same as that reported by the previous AIMD study.[65,94,95] That is, from an initial state of OH^- in coordination with four adjacent water molecules, $OH^-(H_2O)_4$ as shown in Figure 2d, the water coordination number of OH^- is first reduced to form $[HO\cdots H\cdots OH]^-$ (Figure 2e), and then the centered proton hops between the two oxygen atoms due to the thermodynamic fluctuation. Ultimately, OH^- completes the structural diffusion into another 4-fold-coordinated $OH^-(H_2O)_4$ solvent structure and waits for the next proton hopping (Figure 2f). In addition, the diffusion coefficients extracted from our SCAN-based DPMD simulations are 6.0×10^{-9} and 3.0×10^{-9} m^2 s^{-1} for H_3O^+ and OH^- at 330 K, respectively, as shown in Table S4, which are slightly smaller than the experimental measurements ($\sim 9 \times 10^{-9}$ m^2 s^{-1} for H_3O^+ and $\sim 5 \times 10^{-9}$ m^2 s^{-1} for OH^- at ~300 K)[97−99] but agree well with those obtained by CPMD simulations with the SCAN functional (5.7×10^{-9} m^2 s^{-1} for H_3O^+ and 2.9×10^{-9} m^2 s^{-1} for OH^- at 330 K).[81] The obtained diffusion coefficients are sufficient to achieve a dynamic equilibrium state in our 30 ns simulations. Thus, we demonstrated the reliability of the DP model in studying the structural and dynamic properties of water self-ions.

3.2. Distribution of Hydroxide and Hydronium at the Air–Water Interface

3.2.1. Double-Layer Distribution. Using the validated DP model, we carried out DPMD simulations to investigate the equilibrium distribution of water self-ions in several systems (droplet 2, droplet 3, slab 2, and slab 3). No matter whether for a droplet or a slab system, the evolution of the positions of these ions with simulation time demonstrates that the dynamic equilibria of the diffusion processes (Figures S6 and S7) are all reached after 10 ns. As shown in Figure 3a,b, the statistical analysis in the equilibrium interval (10–30 ns) reveals that the maxima of ionic distribution for both hydroxide- and hydronium-containing systems appear within ~1 nm near the average Gibbs dividing surface (GDS). The GDS is a mathematical boundary separating two heterogeneous regions that contain a portion of homogeneous mass on each side,[100] and we approximately define the GDS where the mass density is half that of the bulk water in this work.[9,39,41,72] In particular, H_3O^+ primarily is located at 1.0 Å below the GDS in all systems (close to the topmost layer of the interface), and OH^- mainly accumulates at a depth of 4.9 Å below the GDS. According to the literature, the thickness of the air–water interface is around 0.3–1 nm,[63,101−105] thus, here, we can consider the air–water interface as the region between 2.5 Å above the GDS and 7.5 Å below the GDS. These results indicate that both water self-ions prefer to accumulate in the air–water interface rather than in the bulk at 300 K.

Note that in the present simulations, we did not include the NQEs. It has been reported that the NQEs can soften the water structure by destabilizing the hydrogen bonding network,[88] which is partially similar to the temperature effect. Hence, it is speculated that if NQEs are considered, the ion distribution at 300 K could be closer to that we obtained at 330 K; i.e., when hydronium and hydroxide ions coexist in water, there could be an apparent ionic double-layer distribution with a gap of ~4 Å in the air–water interface, in which H_3O^+ is in the top layer of the interface but OH^- in the lower layer accumulates more charge (~0.1 e/nm^3) than H_3O^+. This explains why the macroscopic experiments

https://doi.org/10.1021/acsphyschemau.3c00076
ACS Phys. Chem Au 2024, 4, 336–346

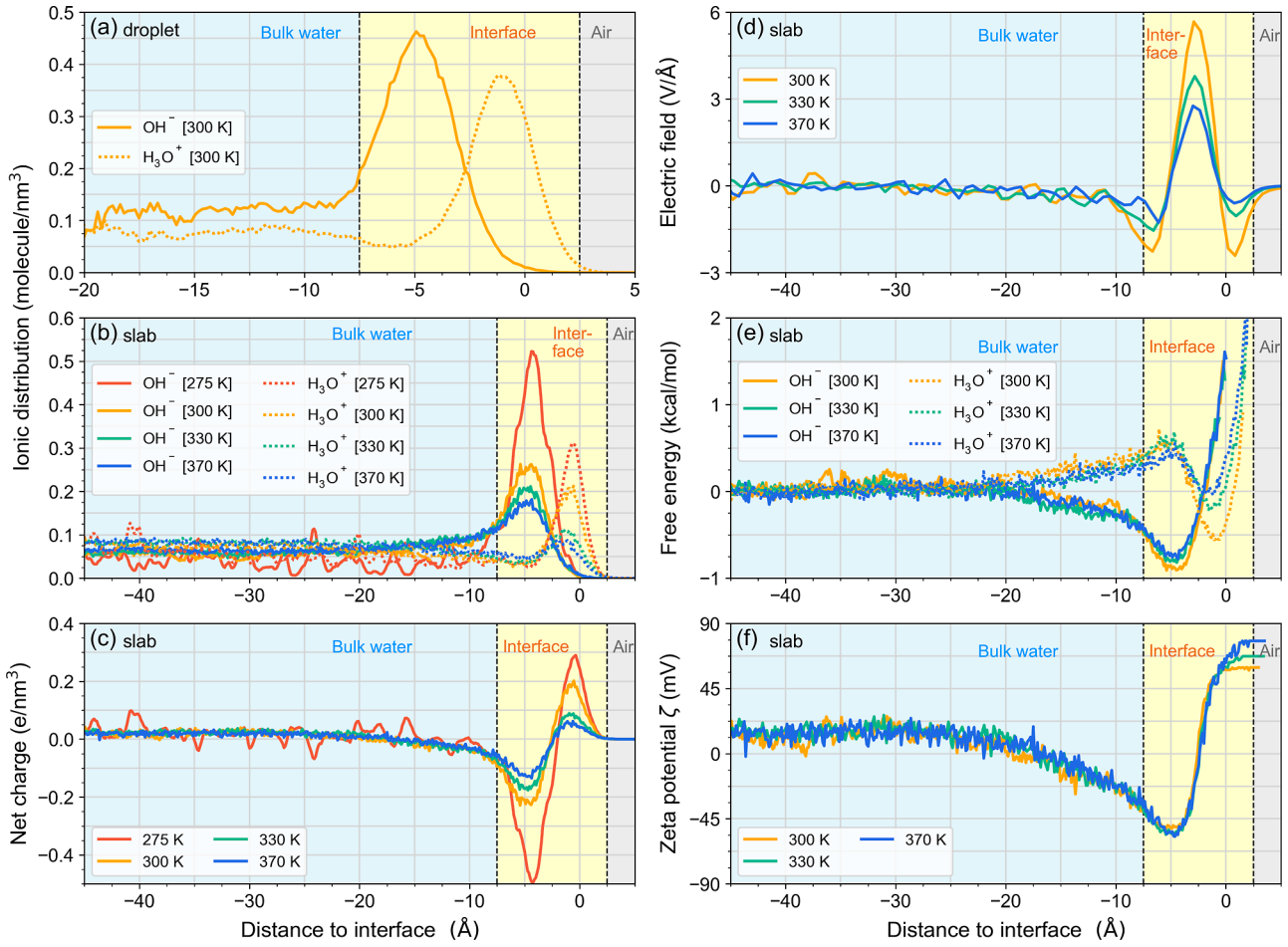

Figure 3. Ionic distribution, electric field, free energy, and zeta potential along the normal distance to the air−water interface. Distribution of hydroxide and hydronium in (a) droplet 2 and droplet 3 systems at 300 K and (b) slab 2 and slab 3 systems at 275−370 K, (c) net charge distribution obtained by combining the ion distributions of slab 2 and slab 3 systems, (d) electric field strength estimated from the net charge distribution, where a negative value means the electric field direction is the same as the interfacial normal vector (from bulk to air) and a positive value means the opposite direction, (e) relative free energy profiles of hydroxide and hydronium along the interfacial depth, and (f) zeta potentials of slab systems estimated from the ion distribution. The normal distances to the interface are defined as being negative on the liquid side, zero at GDS, and positive on the air side. The regions of bulk water, interface, and air are distinguished by different colored backgrounds.

determined the negative charge enrichment at the aqueous interface.

As shown in Figure 3b, the ionic distributions at 275−370 K show a significant temperature effect. When the temperature is increased to 330−370 K from 300 K, the distributions of both ions in the slab systems become slightly more delocalized, especially for hydroniums, which show a relatively weaker dependence of the ionic distribution, with the peak value decreasing around 0.15 e/nm^3. However, the ionic distributions become more localized as the temperature is lowered to 275 K. The net charge in the interface region (−7.5 to 2.5 Å) is negative for all the simulated temperatures (ranging from −0.29 to −0.85 e/nm^3 as shown in Table S5), especially for 275 K (−0.85 e/nm^3). At low temperatures, the molecular thermal motion is reduced, which diminishes the possibility of ions diffusing from the interface back into the bulk, so the phenomenon of ionic double-layer distribution is further strengthened.

As shown in Figure 3c, when simply combining the ionic double-layer distribution in slab 2 and slab 3 systems together to estimate the net charge, the double-layer distribution of net charge can be found at the interface; i.e., positive charges (0.06 to 0.29 e/nm^3) present near ∼−1 Å and then more negative charges (−0.13 to −0.50 e/nm^3) accumulate near ∼−5 Å with respect to the GDS. This distribution further contributes to the presence of the interfacial electric field (Figure 3d). As the temperature drops, we can see the enhanced interfacial electric field strength, and the maxima of electric fields (2.8 to 5.7 V/Å) are located in the middle point (∼−3 Å) of the interface with positive values, which indicate the direction of the electric field from air to bulk. Notably, although the temperatures have spanned from 275 to 370 K, the peaks of the self-ions are still located close to the GDS at different interfacial depths with a separation of ∼4 Å. In addition, Figure 3b shows that the minimum distribution of H_3O^+ and the maximum distribution of OH^- coincide at the same interfacial depth.

Note that the current simulation can handle the $H_3O^+ + OH^- \rightarrow 2H_2O$ recombination reaction, but it is difficult to observe the rare $2H_2O \rightarrow H_3O^+ + OH^-$ water autoionization process without advanced sampling methods. To mitigate the impact of non-neutrality on the findings, we also conducted simulations on a neutral slab 4 system (Table 1). The result confirmed the ionic double-layer distribution we discovered, although statistical information was diminished over time due to rapid recombination reactions (for further details, refer to the Supporting Information). Consequently, to ensure

https://doi.org/10.1021/acsphyschemau.3c00076
ACS Phys. Chem Au 2024, 4, 336−346

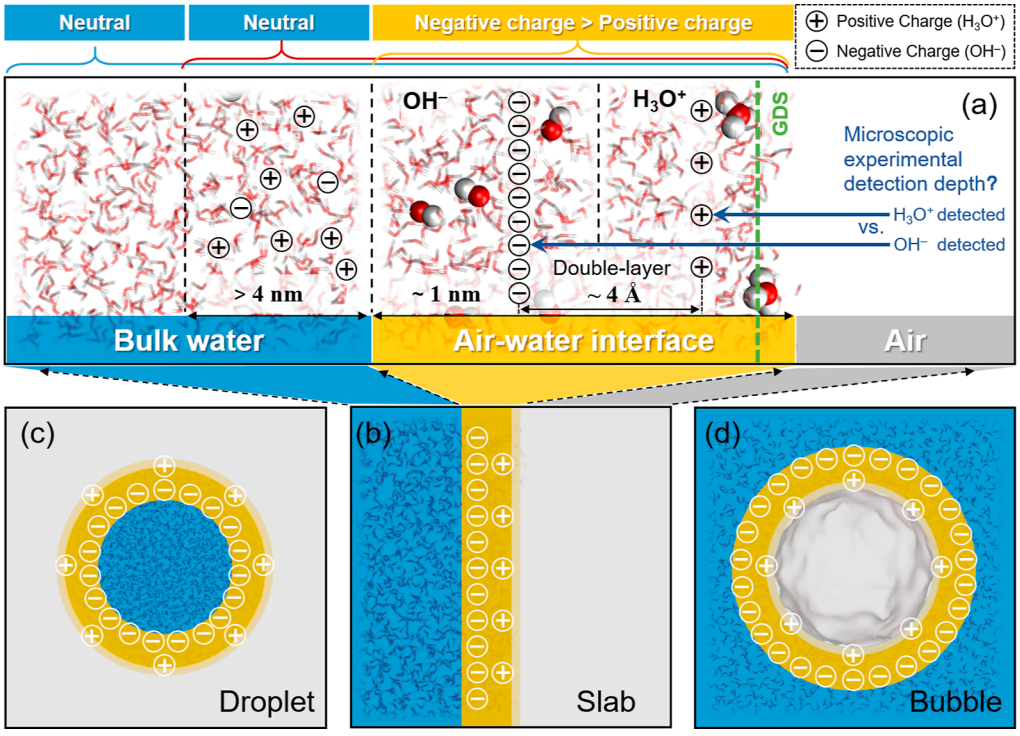

Figure 4. Schematic diagram of double-layer distribution in the air−water interfaces. (a) Zoom-in self-ionic double-layer distribution of the slab system in neutral water. The schematic double-layer distribution in the systems of the (b) water slab, (c) water droplet in air, and (d) air (or vacuum) bubble in water.

sufficient statistical data within the constraints of the simulation timeframe, our discussion primarily is based on simulations with individually sampling self-ions to prevent their recombination.

3.2.2. Interfacial Free Energies and Zeta Potentials. The free energy and zeta potential profiles of the water self-ions as functions of interfacial depths were calculated based on the simulated distribution probabilities for the slab 2 and slab 3 systems. The zeta potential is calculated in the Debye−Hückel approximation,[106,107] which is qualitatively true and reasonable for a qualitative comparison. As depicted in Figure 3e, the free energy profile of H_3O^+ has a minimum at ∼1.0 Å below the GDS, which is also the depth with the maximum H_3O^+ population. This minimum free energy is 0.56 ± 0.24 (0.19 ± 0.08) kcal/mol lower than that in the bulk at 300 (330) K, in reasonable agreement with the interfacial stabilization energy of −1.3 ± 0.2 kcal/mol observed experimentally[44] and with the previously simulated values −0.55 kcal/mol,[41] −0.60 kcal/mol,[43] and −1.0 ± 0.2 kcal/mol[72] at 300 K. Similarly, for OH^-, at the depth of 4.9 Å below the GDS with the maximum population, we also get the lowest free energy, and thus, the interfacial stabilization energy of OH^- is determined to be −0.90 ± 0.10 (−0.81 ± 0.14) kcal/mol at 300 (330) K. The previous simulations predicted slightly smaller interfacial stabilization energies for OH^-, which were −0.6[35] and −0.5 kcal/mol[39] at 300 K.

We also notice that there is a free energy barrier for hydronium diffusion from its optimal distribution depth (1 Å below the GDS) to the bulk, which is 1.13 ± 0.25 (0.81 ± 0.18) kcal/mol at 300 (330) K, and the barrier is coincidentally located at the position (4.9 Å below the GDS) with the lowest free energy of OH^-. All of these results indicate that OH^- has a higher interfacial concentration than H_3O^+, that H_3O^+ tends to be enriched in the topmost layer of the interface, and that once these self-ions occupy their optimal interfacial position, they have to overcome a free energy barrier of ∼1 kcal/mol to diffuse back into the bulk. This means that the double-layer distribution is dynamically stable. The relatively weaker interfacial stabilization energy of H_3O^+ than OH^- also determines the lower H_3O^+ population at the interface. This is why we observe a distribution frequency peak for OH^- higher than that for H_3O^+.

As shown in Figure 3f, a positive zeta potential (∼60 mV) and a negative zeta potential (∼−50 mV) are, respectively, predicted at depths with the maximum populations of H_3O^+ and OH^-. We further estimate the interfacial zeta potential of the neutral water by simply accounting for all ion distribution in the slab 2 and slab 3 systems in the defined interface region (from −7.5 to 2.5 Å), and we get a cumulative zeta potential of −13 mV (−24 mV) at 300 K (330 K), which supports the experimental observation of negative zeta potential for O_2/N_2/air bubbles[22,29,33] and oil droplets.[24,25,33]

3.2.3. Rethinking of the Controversy on the Interfacial Preference of Self-Ions. As far as we know, this finding, that H_3O^+ and OH^- both prefer to accumulate in the air−water interface but at different depths and with a distinction of concentration, has not been fully recognized. As we mentioned in the Introduction section, some previous simulations revealed the adsorption propensity of H_3O^+ at the topmost interfacial layer,[31,34,38,41,43] but others also provided evidence of the slight enhancement of OH^- at the interface[35,39,42] with H_3O^+ avoiding the interface[42] or equally distributing at the interface and in the bulk water.[39] They have come to contradictory conclusions, as have the experimental measurements, so the debate never ends. The present theoretical observation, the double-layer distribution of

https://doi.org/10.1021/acsphyschemau.3c00076
ACS Phys. Chem Au 2024, 4, 336−346

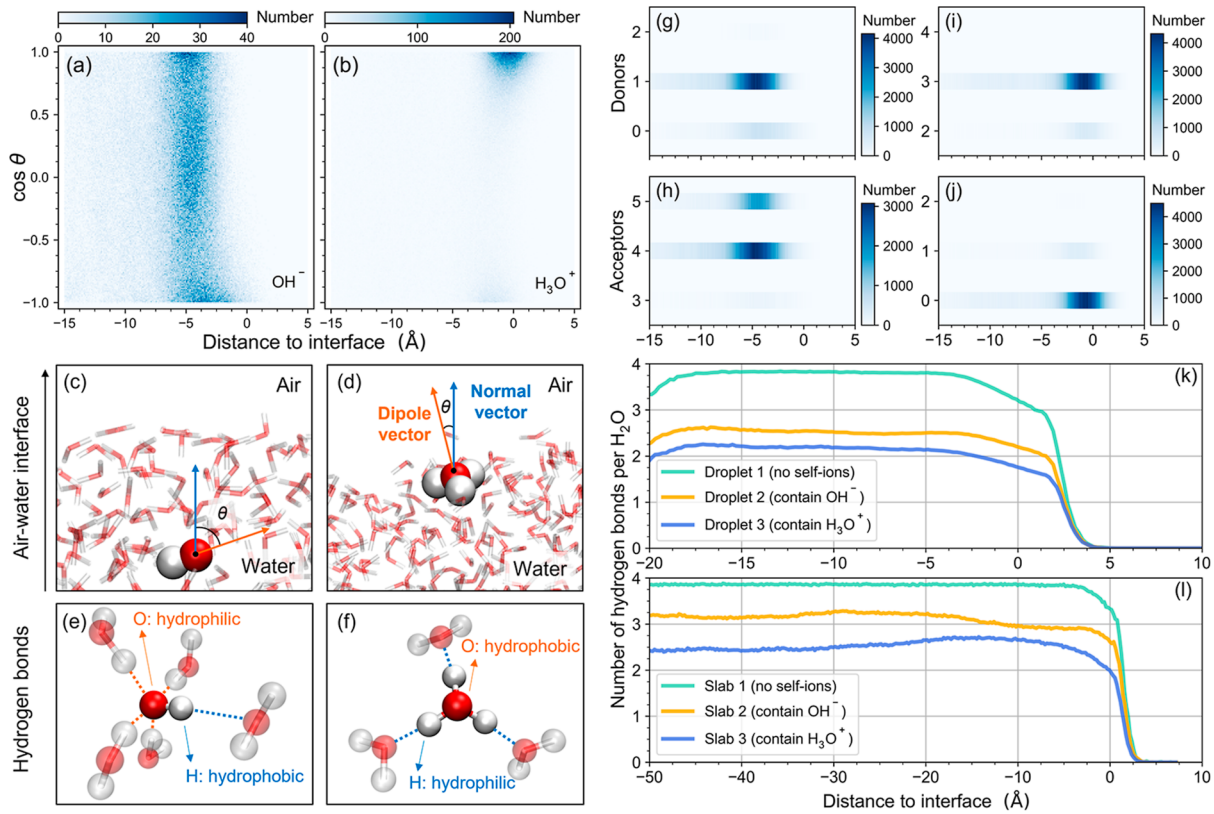

Figure 5. Solvation structures and the hydrogen bond network of water self-ions in the air−water interface. The orientation distributions of (a) hydroxide in the droplet 2 system and (b) hydronium in the droplet 3 system at 300 K. The color bars represent the cumulative number of hydroxides or hydroniums in statistical intervals. The orientation is defined by the cosine of θ angle between the normal vector of the air−water interface and the dipole vector of self-ions, and (c,d) are the schematic examples of the geometric orientation for hydroxide and hydronium, respectively. (e,f) are schematic diagrams of HBs around the amphiphilic hydroxide and hydronium, where the blue and orange dashed lines represent the self-ions being the HB donors and acceptors, respectively. The HB numbers of those acting (g) as HB donors and (h) as HB acceptors for each hydroxide in the droplet 2 system, and the HB numbers of those acting (i) as HB donors and (j) as HB acceptors for each hydronium in the droplet 3 system along various interfacial depths at 300 K, where the color bars represent the cumulative number of donors or acceptors in statistical intervals. The average number of HBs per water molecule as functions of normal distance to the air−water interface in (k) droplet systems and (l) slab systems at 300 K.

hydronium and hydroxide ions at the interface, may help to understand the long-standing controversy about the interfacial propensity of water self-ions. In fact, the speculation of the double-layer distribution has been proposed and discussed by a few groups.[30,32,33] Unfortunately, it did not gather much attention due to the lack of direct evidence. The present work shows that the separation of two ionic layers at the interface is only about 4 Å, which is so narrow that it is difficult to recognize experimentally.

Based on our simulations, we draw schematic diagrams of the ionic double-layer distribution at the air−water interface in Figure 4 for three circumstances, a water slab, a water droplet, and an air (or vacuum) bubble in water, in order to understand the experimental observations. Both OH^- and H_3O^+ in water are attracted toward the interface to form the double-layer distribution with a thickness of ∼1 nm, where the H_3O^+ layer is closer to the air (or vacuum) side compared to the OH^- layer and has a lower ionic concentration due to the lower interfacial stabilization free energy. Although we still cannot assert that this ionic double-layer distribution results in the experimental negative zeta potential, it is certain that microscopic spectroscopic experiments may give opposite results if they detect different interfacial depths. For example, vibrational SFG spectroscopy techniques only provide information in the noncentrosymmetric region.[108] The top layer of the air−water interface breaks the centrosymmetry, and the H_3O^+ adsorption at the top layer shows a different spectroscopy signature than the top layer water, so the interfacial propensity of the proton has been discovered by Das et al.[44] with the vibrational SFG methods. If more advanced techniques are developed to go a little deeper and have a higher spectral resolution, one might see OH^- enrichment in the deeper layer of the interface with a more random orientation.

In addition, note that the air−water interfaces of a water droplet in the air (Figure 4c) and an air bubble in the water (Figure 4d) are both negatively charged, but the structures of the double-layer distribution are opposite due to the different curvature orientations of the gas and liquid phases.

3.3. Reason for the Water Self-Ionic Double-Layer Distribution in the Interface

Next, we further discuss the intrinsic reason for the double-layer distribution of water self-ions in the air−water interface.

In the microscopic view, the orientation distributions (Figure 5a,b) of OH^- ($\cos\theta$ ranges from −1.0 to 1.0) and H_3O^+ ($\cos\theta$ is equal to ∼1.0) at the interface are distinctly different, where the orientation is defined by the cosine of θ angle between the normal vector of the air−water interface and

https://doi.org/10.1021/acsphyschemau.3c00076
ACS Phys. Chem Au 2024, 4, 336−346

the dipole vector of ions (Figure 5c,d). Figure 5a shows that the normal vector of the air−water interface and the dipole vector of H_3O^+ almost overlap, indicating that H_3O^+ ions mainly lie flat on the water surface, with the hydrophobic oxygen atom facing the air. The three hydrophilic protons of H_3O^+ can form three HBs with three neighboring water molecules (Figure 5f,i), which is consistent with previous works.[43,52,109] In this orientation, H_3O^+ is more stable at the topmost layer of the interface because its hydrophobic oxygen, which hardly acts as an HB acceptor (Figure 5j) due to having fewer lone-pair electrons, is pushed toward the interface to keep a better HB network of the bulk water. It also explains why the temperature effect and the nuclear quantum effect, both of which soften the HB network, will weaken the interfacial preference of H_3O^+, as we observed in Figure 3b.

Similar to the hydronium, OH^- also has amphiphilic behaviors.[81,99,110] Considering this, one could assume that the orientation of OH^- in the air−water interface might be like that of H_3O^+, i.e., the hydrophilic oxygen toward the liquid phase and the hydrophobic hydrogen toward the gas phase. However, the fact is that such conformations ($\cos\theta = -1.0$) account for only a small fraction as depicted in Figure 5a. This is because the hydrophobic hydrogen of OH^- can also act as the HB donor to interact with one water molecule (Figure 5g), leading to the relatively weaker hydrophobicity of OH^- than that of H_3O^+. The hydrophilic oxygen, which has more lone-pair electrons than the oxygen of neutral water molecules, can act as an HB acceptor to form HBs with 3−5 water molecules[38,95,110] (see Figure 5e,h). The abundant HB network arises from the delocalization of oxygen lone-pair electrons, forming a stable dynamic hyper-coordination solvation structure of OH^-,[95,110] so the orientation of OH^- is randomly distributed.

Although the OH^- can form more HBs than H_3O^+, it also weakens the overall HB network of bulk water as shown in Figure 5k,l, and consequently, it is attracted to the interface with the partially broken HB network to reduce the disruption to the HB structure of bulk water. At the same time, the hyper-coordination solvation structure of OH^- keeps it away from the topmost layer of the interface (where H_3O^+ preferentially occupies), and instead OH^- prefers to accumulate at the interfacial depth of 2−4 water-molecule layers below the GDS (Figure 5c). Thus, the double-layer distribution of water self-ions in the interfaces can eventually form when thermodynamic equilibrium is reached.

4. CONCLUSIONS

In this work, we trained an accurate deep potential model for hydroxide- and hydronium-containing water systems based on the DFT calculations with the SCAN functional and then performed DPMD simulations to study the distribution of water self-ions in water droplet and slab systems. We found that both OH^- and H_3O^+ tend to accumulate in the air−water interface but at a different depth, leading to an ionic double-layer distribution at the interface. The interfacial propensity arises from the amphipathy of the water self-ions; the distinct stable solvation structures determine that they preferentially occupy different interfacial depths: H_3O^+ with a strongly hydrophobic oxygen atom is closer to the water surface, in agreement with most microscopic studies, OH^- with a hyper-coordination solvation structure prefers to locate at a deeper interfacial depth, and the gap between the two ion layers is only ∼4 Å. As compared to H_3O^+, OH^- has a higher interfacial stabilization free energy and consequently a higher concentration in the interface.

Notably, we specifically conducted separate simulations for systems containing hydronium and hydroxide ions to prevent ionic recombination into water molecules and to ensure adequate sampling within a limited simulation time frame and a smaller box size compared to real-world conditions. Furthermore, the DP model is based on local environmental features and does not account for a specific long-range electrostatic interaction term. As a result, the current finding regarding the ionic double-layer distribution may offer a qualitatively (albeit not quantitatively) self-consistent explanation between previous macroscopic and microscopic studies of the interfacial distribution. Efforts should be made to address these limitations in future simulations in order to conduct a more comprehensive examination of the air−water interface. Fortunately, recent high-level heterodyne-detected vibrational SFG results for electrolyte solutions may have partly corroborated our findings, providing indirect experimental evidence of ionic double-layer distribution,[111] but the challenge of directly detecting the ionic preference at a pure air−water interface should be addressed in the future experiments.

■ ASSOCIATED CONTENT

Data Availability Statement

The input files required to replicate the research are accessible at https://github.com/Zhang-pchao/DoubleLayerAirWater.

Supporting Information

The Supporting Information is available free of charge at https://pubs.acs.org/doi/10.1021/acsphyschemau.3c00076.

DP model training and data set building, validation of the DP model, distribution of the hydroxide and hydronium, zeta potential, electric field, pH and pOH, surface tension, surface excess, free energy, and hydrogen bonding network of hydroxide and hydronium (PDF)

■ AUTHOR INFORMATION

Corresponding Author

Xuefei Xu − *Center for Combustion Energy, Department of Energy and Power Engineering, and Key Laboratory for Thermal Science and Power Engineering of Ministry of Education, Tsinghua University, Beijing 100084, China;* orcid.org/0000-0002-2009-0483; Email: xuxuefei@tsinghua.edu.cn

Authors

Pengchao Zhang − *Center for Combustion Energy, Department of Energy and Power Engineering, and Key Laboratory for Thermal Science and Power Engineering of Ministry of Education, Tsinghua University, Beijing 100084, China;* orcid.org/0000-0002-6556-6588

Muye Feng − *School of Mechanical and Power Engineering, Nanjing Tech University, Nanjing 211816, China;* orcid.org/0000-0003-4050-8901

Complete contact information is available at: https://pubs.acs.org/10.1021/acsphyschemau.3c00076

Author Contributions

CRediT: **Pengchao Zhang:** conceptualization, methodology, software, validation, formal analysis, investigation, writing—original draft, writing—review and editing, visualization. **Muye Feng:** methodology, visualization, validation. **Xuefei Xu:** conceptualization, supervision, writing—original draft, writing—review and editing, funding acquisition, project administration.

Notes

The authors declare no competing financial interest.

■ ACKNOWLEDGMENTS

The authors are very grateful to Professor Michele Parrinello, Professor Xiao He, Professor Chao Sun, Professor Mingbo Li, Xiaotong Ma, and Axel Tosello Gardini for their helpful discussion. This work was supported in part by the National Natural Science Foundation of China (grant nos. 21973053, 11988102, and 52106164). A part of the computation was completed at the High Performance Computing Platform of Tsinghua University.

■ REFERENCES

(1) Ruiz-Lopez, M. F.; Francisco, J. S.; Martins-Costa, M. T.; Anglada, J. M. Molecular Reactions at Aqueous Interfaces. *Nat. Rev. Chem.* **2020**, *4*, 459−475.
(2) Gonella, G.; Backus, E. H.; Nagata, Y.; Bonthuis, D. J.; Loche, P.; Schlaich, A.; Netz, R. R.; Kühnle, A.; McCrum, I. T.; Koper, M. T.; et al. Water at Charged Interfaces. *Nat. Rev. Chem.* **2021**, *5*, 466−485.
(3) Chao, Y.; Shum, H. C. Emerging Aqueous Two-Phase Systems: From Fundamentals of Interfaces to Biomedical Applications. *Chem. Soc. Rev.* **2020**, *49*, 114−142.
(4) Groß, A.; Sakong, S. *Ab Initio* Simulations of Water/Metal Interfaces. *Chem. Rev.* **2022**, *122*, 10746−10776.
(5) Wei, Z.; Li, Y.; Cooks, R. G.; Yan, X. Accelerated Reaction Kinetics in Microdroplets: Overview and Recent Developments. *Annu. Rev. Phys. Chem.* **2020**, *71*, 31−51.
(6) Xiong, H.; Lee, J. K.; Zare, R. N.; Min, W. Strong Electric Field Observed at the Interface of Aqueous Microdroplets. *J. Phys. Chem. Lett.* **2020**, *11*, 7423−7428.
(7) Chamberlayne, C. F.; Zare, R. N. Simple Model for the Electric Field and Spatial Distribution of Ions in a Microdroplet. *J. Chem. Phys.* **2020**, *152*, 184702.
(8) Hao, H.; Leven, I.; Head-Gordon, T. Can Electric Fields Drive Chemistry for an Aqueous Microdroplet? *Nat. Commun.* **2022**, *13*, 280.
(9) Martins-Costa, M. T.; Ruiz-López, M. F. Electrostatics and Chemical Reactivity at the Air-Water Interface. *J. Am. Chem. Soc.* **2023**, *145*, 1400−1406.
(10) Li, Y.; Chen, Y.-X.; Liu, Z.-F. OH^{-}··· Au Hydrogen Bond and Its Effect on the Oxygen Reduction Reaction on Au (100) in Alkaline Media. *J. Phys. Chem. Lett.* **2022**, *13*, 9035−9043.
(11) Zhong, G.; Cheng, T.; Shah, A. H.; Wan, C.; Huang, Z.; Wang, S.; Leng, T.; Huang, Y.; Goddard, W. A.; Duan, X. Determining the Hydronium pK_a at Platinum Surfaces and the Effect on pH-Dependent Hydrogen Evolution Reaction Kinetics. *Proc. Natl. Acad. Sci. U.S.A.* **2022**, *119*, No. e2208187119.
(12) Lee, J. K.; Walker, K. L.; Han, H. S.; Kang, J.; Prinz, F. B.; Waymouth, R. M.; Nam, H. G.; Zare, R. N. Spontaneous Generation of Hydrogen Peroxide from Aqueous Microdroplets. *Proc. Natl. Acad. Sci. U.S.A.* **2019**, *116*, 19294−19298.
(13) Jin, S.; Chen, H.; Yuan, X.; Xing, D.; Wang, R.; Zhao, L.; Zhang, D.; Gong, C.; Zhu, C.; Gao, X.; et al. The Spontaneous Electron-Mediated Redox Processes on Sprayed Water Microdroplets. *JACS Au* **2023**, *3*, 1563−1571.
(14) Colussi, A. J. Mechanism of Hydrogen Peroxide Formation on Sprayed Water Microdroplets. *J. Am. Chem. Soc.* **2023**, *145*, 16315−16317.
(15) Song, X.; Basheer, C.; Zare, R. N. Making Ammonia from Nitrogen and Water Microdroplets. *Proc. Natl. Acad. Sci. U.S.A.* **2023**, *120*, No. e2301206120.
(16) Cassone, G.; Saija, F.; Sponer, J.; Shaik, S. The Reactivity-Enhancing Role of Water Clusters in Ammonia Aqueous Solutions. *J. Phys. Chem. Lett.* **2023**, *14*, 7808−7813.
(17) Liu, Y.; Ge, Q.; Wang, T.; Zhang, R.; Li, K.; Gong, K.; Xie, L.; Wang, W.; Wang, L.; You, W.; et al. Strong Electric Field Force at the Air/Water Interface Drives Fast Sulfate Production in the Atmosphere. *Chem* **2024**, *10*, 330−351.
(18) Meng, Y.; Zare, R. N.; Gnanamani, E. One-Step, Catalyst-Free Formation of Phenol from Benzoic Acid Using Water Microdroplets. *J. Am. Chem. Soc.* **2023**, *145*, 19202−19206.
(19) Cheng, Y.; Xu, X.; Wang, M.; Deng, C.; Sun, Y.; Yan, C.; Qian, T. Interfacial Proton Supply/Filtration Regulates the Dynamics of Electrocatalytic Nitrogen Reduction Reaction: A Perspective. *Adv. Funct. Mater.* **2023**, *33*, 2302332.
(20) Döpke, M. F.; Westerbaan van der Meij, F.; Coasne, B.; Hartkamp, R. Surface Protolysis and Its Kinetics Impact the Electrical Double Layer. *Phys. Rev. Lett.* **2022**, *128*, 056001.
(21) Quincke, G. Ueber die Fortführung materieller Theilchen durch strömende Elektricität. *Ann. Phys.* **1861**, *189* (8), 513−598.
(22) Graciaa, A.; Morel, G.; Saulner, P.; Lachaise, J.; Schechter, R. The ζ-Potential of Gas Bubbles. *J. Colloid Interface Sci.* **1995**, *172*, 131−136.
(23) Weissenborn, P. K.; Pugh, R. J. Surface Tension of Aqueous Solutions of Electrolytes: Relationship with Ion Hydration, Oxygen Solubility, and Bubble Coalescence. *J. Colloid Interface Sci.* **1996**, *184*, 550−563.
(24) Marinova, K.; Alargova, R.; Denkov, N.; Velev, O.; Petsev, D.; Ivanov, I.; Borwankar, R. Charging of Oil−Water Interfaces Due to Spontaneous Adsorption of Hydroxyl Ions. *Langmuir* **1996**, *12*, 2045−2051.
(25) Beattie, J. K.; Djerdjev, A. M. The Pristine Oil/Water Interface: Surfactant-Free Hydroxide-Charged Emulsions. *Angew. Chem., Int. Ed.* **2004**, *43*, 3568−3571.
(26) Takahashi, M. ζ Potential of Microbubbles in Aqueous Solutions: Electrical Properties of the Gas-Water Interface. *J. Phys. Chem. B* **2005**, *109*, 21858−21864.
(27) Petersen, P. B.; Saykally, R. J. Evidence for an Enhanced Hydronium Concentration at the Liquid Water Surface. *J. Phys. Chem. B* **2005**, *109*, 7976−7980.
(28) Jungwirth, P.; Tobias, D. J. Specific Ion Effects at the Air/Water Interface. *Chem. Rev.* **2006**, *106*, 1259−1281.
(29) Creux, P.; Lachaise, J.; Graciaa, A.; Beattie, J. K. Specific Cation Effects at the Hydroxide-Charged Air/Water Interface. *J. Phys. Chem. C* **2007**, *111*, 3753−3755.
(30) Vácha, R.; Buch, V.; Milet, A.; Devlin, J. P.; Jungwirth, P. Autoionization at the Surface of Pure Water: Is the Top Layer pH Neutral, Basic, or Acidic? *Phys. Chem. Chem. Phys.* **2007**, *9*, 4736−4747.
(31) Buch, V.; Milet, A.; Vácha, R.; Jungwirth, P.; Devlin, J. P. Water Surface is Acidic. *Proc. Natl. Acad. Sci. U.S.A.* **2007**, *104*, 7342−7347.
(32) Beattie, J. K.; Djerdjev, A. M.; Warr, G. G. The Surface of Neat Water is Basic. *Faraday Discuss.* **2009**, *141*, 31−39.
(33) Creux, P.; Lachaise, J.; Graciaa, A.; Beattie, J. K.; Djerdjev, A. M. Strong Specific Hydroxide Ion Binding at the Pristine Oil/Water and Air/Water Interfaces. *J. Phys. Chem. B* **2009**, *113*, 14146−14150.
(34) Lee, H.-S.; Tuckerman, M. E. *Ab Initio* Molecular Dynamics Studies of the Liquid-Vapor Interface of an HCl Solution. *J. Phys. Chem. A* **2009**, *113*, 2144−2151.
(35) Mundy, C. J.; Kuo, I.-F. W.; Tuckerman, M. E.; Lee, H.-S.; Tobias, D. J. Hydroxide Anion at the Air−Water Interface. *Chem. Phys. Lett.* **2009**, *481*, 2−8.
(36) Mishra, H.; Enami, S.; Nielsen, R. J.; Stewart, L. A.; Hoffmann, M. R.; Goddard, W. A.; Colussi, A. J. Brønsted Basicity of the Air−

https://doi.org/10.1021/acsphyschemau.3c00076
ACS Phys. Chem Au 2024, 4, 336−346

Water Interface. *Proc. Natl. Acad. Sci. U.S.A.* **2012**, *109*, 18679−18683.
(37) Saykally, R. J. Two Sides of the Acid-Base Story. *Nat. Chem.* **2013**, *5*, 82−84.
(38) Hub, J. S.; Wolf, M. G.; Caleman, C.; van Maaren, P. J.; Groenhof, G.; van der Spoel, D. Thermodynamics of Hydronium and Hydroxide Surface Solvation. *Chem. Sci.* **2014**, *5*, 1745−1749.
(39) Baer, M. D.; Kuo, I.-F. W.; Tobias, D. J.; Mundy, C. J. Toward a Unified Picture of the Water Self-Ions at the Air−Water Interface: A Density Functional Theory Perspective. *J. Phys. Chem. B* **2014**, *118*, 8364−8372.
(40) Fang, H.; Wu, W.; Sang, Y.; Chen, S.; Zhu, X.; Zhang, L.; Niu, Y.; Gan, W. Evidence of the Adsorption of Hydroxide Ion at Hexadecane/Water Interface from Second Harmonic Generation Study. *RSC Adv.* **2015**, *5*, 23578−23585.
(41) Tse, Y.-L. S.; Chen, C.; Lindberg, G. E.; Kumar, R.; Voth, G. A. Propensity of Hydrated Excess Protons and Hydroxide Anions for the Air−Water Interface. *J. Am. Chem. Soc.* **2015**, *137*, 12610−12616.
(42) Bai, C.; Herzfeld, J. Surface Propensities of the Self-Ions of Water. *ACS Cent. Sci.* **2016**, *2*, 225−231.
(43) Mamatkulov, S. I.; Allolio, C.; Netz, R. R.; Bonthuis, D. J. Orientation-Induced Adsorption of Hydrated Protons at the Air−Water Interface. *Angew. Chem., Int. Ed.* **2017**, *56*, 15846−15851.
(44) Das, S.; Imoto, S.; Sun, S.; Nagata, Y.; Backus, E. H.; Bonn, M. Nature of Excess Hydrated Proton at the Water−Air Interface. *J. Am. Chem. Soc.* **2020**, *142*, 945−952.
(45) Colussi, A. J.; Enami, S.; Ishizuka, S. Hydronium Ion Acidity Above and Below the Interface of Aqueous Microdroplets. *ACS Earth Space Chem.* **2021**, *5*, 2341−2346.
(46) Agmon, N.; Bakker, H. J.; Campen, R. K.; Henchman, R. H.; Pohl, P.; Roke, S.; Thämer, M.; Hassanali, A. Protons and Hydroxide Ions in Aqueous Systems. *Chem. Rev.* **2016**, *116*, 7642−7672.
(47) Pletincx, S.; Fockaert, L. L. I.; Mol, J. M.; Hauffman, T.; Terryn, H. Probing the Formation and Degradation of Chemical Interactions from Model Molecule/Metal Oxide to Buried Polymer/Metal Oxide Interfaces. *npj Mater. Degrad.* **2019**, *3*, 23.
(48) Gong, K.; Ao, J.; Li, K.; Liu, L.; Liu, Y.; Xu, G.; Wang, T.; Cheng, H.; Wang, Z.; Zhang, X.; et al. Imaging of pH Distribution Inside Individual Microdroplet by Stimulated Raman Microscopy. *Proc. Natl. Acad. Sci. U.S.A.* **2023**, *120*, No. e2219588120.
(49) Wei, H.; Vejerano, E. P.; Leng, W.; Huang, Q.; Willner, M. R.; Marr, L. C.; Vikesland, P. J. Aerosol Microdroplets Exhibit a Stable pH Gradient. *Proc. Natl. Acad. Sci. U.S.A.* **2018**, *115*, 7272−7277.
(50) Li, M.; Kan, Y.; Su, H.; Pöschl, U.; Parekh, S. H.; Bonn, M.; Cheng, Y. Spatial Homogeneity of pH in Aerosol Microdroplets. *Chem* **2023**, *9*, 1036−1046.
(51) Rehl, B.; Ma, E.; Parshotam, S.; DeWalt-Kerian, E. L.; Liu, T.; Geiger, F. M.; Gibbs, J. M. Water Structure in the Electrical Double Layer and the Contributions to the Total Interfacial Potential at Different Surface Charge Densities. *J. Am. Chem. Soc.* **2022**, *144*, 16338−16349.
(52) Tian, C.; Ji, N.; Waychunas, G. A.; Shen, Y. R. Interfacial Structures of Acidic and Basic Aqueous Solutions. *J. Am. Chem. Soc.* **2008**, *130*, 13033−13039.
(53) Jena, K. C.; Covert, P. A.; Hore, D. K. The Effect of Salt on the Water Structure at a Charged Solid Surface: Differentiating Second- and Third-Order Nonlinear Contributions. *J. Phys. Chem. Lett.* **2011**, *2*, 1056−1061.
(54) Gonella, G.; Lütgebaucks, C.; De Beer, A. G.; Roke, S. Second Harmonic and Sum-Frequency Generation from Aqueous Interfaces is Modulated by Interference. *J. Phys. Chem. C* **2016**, *120*, 9165−9173.
(55) Yu, C.-C.; Seki, T.; Wang, Y.; Bonn, M.; Nagata, Y. Polarization-Dependent Sum-Frequency Generation Spectroscopy for Ångstrom-Scale Depth Profiling of Molecules at Interfaces. *Phys. Rev. Lett.* **2022**, *128*, 226001.
(56) Du, Q.; Freysz, E.; Shen, Y. R. Vibrational Spectra of Water Molecules at Quartz/Water Interfaces. *Phys. Rev. Lett.* **1994**, *72*, 238−241.
(57) Inoue, K.-i.; Nihonyanagi, S.; Singh, P. C.; Yamaguchi, S.; Tahara, T. 2D Heterodyne-Detected Sum Frequency Generation Study on the Ultrafast Vibrational Dynamics of H_2O and HOD Water at Charged Interfaces. *J. Chem. Phys.* **2015**, *142*, 212431.
(58) Inoue, K.-i.; Ahmed, M.; Nihonyanagi, S.; Tahara, T. Reorientation-Induced Relaxation of Free OH at the Air/Water Interface Revealed by Ultrafast Heterodyne-Detected Nonlinear Spectroscopy. *Nat. Commun.* **2020**, *11*, 5344.
(59) Montenegro, A.; Dutta, C.; Mammetkuliev, M.; Shi, H.; Hou, B.; Bhattacharyya, D.; Zhao, B.; Cronin, S. B.; Benderskii, A. V. Asymmetric Response of Interfacial Water to Applied Electric Fields. *Nature* **2021**, *594*, 62−65.
(60) Montenegro, A.; Vaughn, A. E.; Mammetkuliyev, M.; Zhao, B.; Zhang, B.; Shi, H.; Bhattacharyya, D.; Benderskii, A. V.; Cronin, S. B. Field-Dependent Orientation and Free Energy of D_2O at an Electrode Surface Observed via SFG Spectroscopy. *J. Phys. Chem. C* **2022**, *126*, 20831−20839.
(61) Somorjai, G. A.; Park, J. Y. Molecular Surface Chemistry by Metal Single Crystals and Nanoparticles from Vacuum to High Pressure. *Chem. Soc. Rev.* **2008**, *37*, 2155−2162.
(62) Zaera, F. Probing Liquid/Solid Interfaces at the Molecular Level. *Chem. Rev.* **2012**, *112*, 2920−2986.
(63) Tang, F.; Ohto, T.; Sun, S.; Rouxel, J. R.; Imoto, S.; Backus, E. H.; Mukamel, S.; Bonn, M.; Nagata, Y. Molecular Structure and Modeling of Water−Air and Ice−Air Interfaces Monitored by Sum-Frequency Generation. *Chem. Rev.* **2020**, *120*, 3633−3667.
(64) Sakunkaewkasem, S.; Deleon, D.; Choi, Y.; Tran, H.-V.; Marquez, M. D.; Baldelli, S.; Lee, T. R. Sum Frequency Generation Spectroscopy of Fluorinated Organic Material-Based Interfaces: A Tutorial Review. *Analyst* **2023**, *148*, 2901−2920.
(65) Marx, D. Proton Transfer 200 Years After Von Grotthuss: Insights from *Ab Initio* Simulations. *ChemPhysChem* **2006**, *7*, 1848−1870.
(66) de Grotthuss, C. J. T. Mémoire sur la Décomposition de l'Eau et des Corps qu'elle Tient en Dissolution à l'Aide de l'Électricité Galvanique. *Ann. Chim.* **1806**, *58*, 54−74.
(67) Blank, T. B.; Brown, S. D.; Calhoun, A. W.; Doren, D. J. Neural Network Models of Potential Energy Surfaces. *J. Chem. Phys.* **1995**, *103*, 4129−4137.
(68) Behler, J.; Parrinello, M. Generalized Neural Network Representation of High-Dimensional Potential-Energy Surfaces. *Phys. Rev. Lett.* **2007**, *98*, 146401.
(69) Wang, H.; Zhang, L.; Han, J.; Weinan, E. DeePMD-kit: A Deep Learning Package for Many-Body Potential Energy Representation and Molecular Dynamics. *Comput. Phys. Commun.* **2018**, *228*, 178−184.
(70) Zeng, J.; Zhang, D.; Lu, D.; Mo, P.; Li, Z.; Chen, Y.; Rynik, M.; Huang, L.; Li, Z.; Shi, S.; et al. DeePMD-kit v2: A Software Package for Deep Potential Models. *J. Chem. Phys.* **2023**, *159*, 054801.
(71) Schütt, K. T.; Sauceda, H. E.; Kindermans, P.-J.; Tkatchenko, A.; Müller, K. R. SchNet−A Deep Learning Architecture for Molecules and Materials. *J. Chem. Phys.* **2018**, *148*, 241722.
(72) de la Puente, M.; David, R.; Gomez, A.; Laage, D. Acids at the Edge: Why Nitric and Formic Acid Dissociations at Air−Water Interfaces Depend on Depth and on Interface Specific Area. *J. Am. Chem. Soc.* **2022**, *144*, 10524−10529.
(73) Galib, M.; Limmer, D. T. Reactive Uptake of N_2O_5 by Atmospheric Aerosol is Dominated by Interfacial Processes. *Science* **2021**, *371*, 921−925.
(74) Calegari Andrade, M. F.; Ko, H.-Y.; Zhang, L.; Car, R.; Selloni, A. Free Energy of Proton Transfer at the Water−TiO_2 Interface from *Ab Initio* Deep Potential Molecular Dynamics. *Chem. Sci.* **2020**, *11*, 2335−2341.
(75) Wen, T.; Zhang, L.; Wang, H.; Weinan, E.; Srolovitz, D. J. Deep Potentials for Materials Science. *Mater. Futures* **2022**, *1*, 022601.
(76) Piaggi, P. M.; Weis, J.; Panagiotopoulos, A. Z.; Debenedetti, P. G.; Car, R. Homogeneous Ice Nucleation in an *Ab Initio* Machine-Learning Model of Water. *Proc. Natl. Acad. Sci. U.S.A.* **2022**, *119*, No. e2207294119.

https://doi.org/10.1021/acsphyschemau.3c00076
ACS Phys. Chem Au 2024, 4, 336−346

(77) Zhang, L.; Wang, H.; Car, R.; Weinan, E. Phase Diagram of a Deep Potential Water Model. *Phys. Rev. Lett.* **2021**, *126*, 236001.
(78) Xu, J.; Zhang, C.; Zhang, L.; Chen, M.; Santra, B.; Wu, X. Isotope Effects in Molecular Structures and Electronic Properties of Liquid Water via Deep Potential Molecular Dynamics Based on the SCAN Functional. *Phys. Rev. B* **2020**, *102*, 214113.
(79) Ko, H.-Y.; Zhang, L.; Santra, B.; Wang, H.; E, W.; DiStasio Jr, R. A.; Car, R. Isotope Effects in Liquid Water via Deep Potential Molecular Dynamics. *Mol. Phys.* **2019**, *117*, 3269−3281.
(80) Sun, J.; Ruzsinszky, A.; Perdew, J. P. Strongly Constrained and Appropriately Normed Semilocal Density Functional. *Phys. Rev. Lett.* **2015**, *115*, 036402.
(81) Liu, R.; Zhang, C.; Liang, X.; Liu, J.; Wu, X.; Chen, M. Structural and Dynamic Properties of Solvated Hydroxide and Hydronium Ions in Water from *Ab Initio* Modeling. *J. Chem. Phys.* **2022**, *157*, 024503.
(82) Zheng, L.; Chen, M.; Sun, Z.; Ko, H.-Y.; Santra, B.; Dhuvad, P.; Wu, X. Structural, Electronic, and Dynamical Properties of Liquid Water by *Ab Initio* Molecular Dynamics Based on SCAN Functional Within the Canonical Ensemble. *J. Chem. Phys.* **2018**, *148*, 164505.
(83) Chen, M.; Ko, H. Y.; Remsing, R. C.; Calegari Andrade, M. F.; Santra, B.; Sun, Z.; Selloni, A.; Car, R.; Klein, M. L.; Perdew, J. P.; et al. *Ab Initio* Theory and Modeling of Water. *Proc. Natl. Acad. Sci. U.S.A.* **2017**, *114*, 10846−10851.
(84) Zhang, Y.; Wang, H.; Chen, W.; Zeng, J.; Zhang, L.; Wang, H.; Weinan, E. DP-GEN: A Concurrent Learning Platform for the Generation of Reliable Deep Learning Based Potential Energy Models. *Comput. Phys. Commun.* **2020**, *253*, 107206.
(85) Plimpton, S. Fast Parallel Algorithms for Short-Range Molecular Dynamics. *J. Comput. Phys.* **1995**, *117*, 1−19.
(86) Kresse, G.; Furthmüller, J. Efficient Iterative Schemes for *Ab Initio* Total-Energy Calculations Using a Plane-Wave Basis Set. *Phys. Rev. B* **1996**, *54*, 11169−11186.
(87) Kresse, G.; Furthmüller, J. Efficiency of Ab-Initio Total Energy Calculations for Metals and Semiconductors Using a Plane-Wave Basis Set. *Comput. Mater. Sci.* **1996**, *6*, 15−50.
(88) Morrone, J. A.; Car, R. Nuclear Quantum Effects in Water. *Phys. Rev. Lett.* **2008**, *101*, 017801.
(89) Nosé, S. A Unified Formulation of the Constant Temperature Molecular Dynamics Methods. *J. Chem. Phys.* **1984**, *81*, 511−519.
(90) Hoover, W. G. Canonical Dynamics: Equilibrium Phase-space Distributions. *Phys. Rev. A* **1985**, *31*, 1695−1697.
(91) Humphrey, W.; Dalke, A.; Schulten, K. VMD: Visual Molecular Dynamics. *J. Mol. Graph.* **1996**, *14*, 33−38.
(92) Hunter, J. D. Matplotlib: A 2D Graphics Environment. *Comput. Sci. Eng.* **2007**, *9*, 90−95.
(93) Michaud-Agrawal, N.; Denning, E. J.; Woolf, T. B.; Beckstein, O. MDAnalysis: A Toolkit for the Analysis of Molecular Dynamics Simulations. *J. Comput. Chem.* **2011**, *32*, 2319−2327.
(94) Tuckerman, M. E.; Marx, D.; Parrinello, M. The Nature and Transport Mechanism of Hydrated Hydroxide Ions in Aqueous Solution. *Nature* **2002**, *417*, 925−929.
(95) Marx, D.; Chandra, A.; Tuckerman, M. E. Aqueous Basic Solutions: Hydroxide Solvation, Structural Diffusion, and Comparison to the Hydrated Proton. *Chem. Rev.* **2010**, *110*, 2174−2216.
(96) Tian, Y.; Hong, J.; Cao, D.; You, S.; Song, Y.; Cheng, B.; Wang, Z.; Guan, D.; Liu, X.; Zhao, Z.; et al. Visualizing Eigen/Zundel Cations and Their Interconversion in Monolayer Water on Metal Surfaces. *Science* **2022**, *377*, 315−319.
(97) Halle, B.; Karlström, G. Prototropic Charge Migration in Water. Part 2.—Interpretation of Nuclear Magnetic Resonance and Conductivity Data in Terms of Model Mechanisms. *J. Chem. Soc., Faraday Trans. 2* **1983**, *79*, 1047−1073.
(98) Sluyters, J.; Sluyters-Rehbach, M. The Mechanism of the Hydrogen Ion Conduction in Liquid Light and Heavy Water Derived from the Temperature Dependence of Their Limiting Conductivities. *J. Phys. Chem. B* **2010**, *114*, 15582−15589.
(99) Chen, M.; Zheng, L.; Santra, B.; Ko, H.-Y.; DiStasio Jr, R. A.; Klein, M. L.; Car, R.; Wu, X. Hydroxide Diffuses Slower Than Hydronium in Water Because Its Solvated Structure Inhibits Correlated Proton Transfer. *Nat. Chem.* **2018**, *10*, 413−419.
(100) Gibbs, J. W. *The Collected Works of J. Willard Gibbs*; Longmans, Green, 1928.
(101) McBain, J.; Bacon, R.; Bruce, H. Optical Surface Thickness of Pure Water. *J. Chem. Phys.* **1939**, *7*, 818−823.
(102) Braslau, A.; Deutsch, M.; Pershan, P. S.; Weiss, A.; Als-Nielsen, J.; Bohr, J. Surface Roughness of Water Measured by X-Ray Reflectivity. *Phys. Rev. Lett.* **1985**, *54*, 114−117.
(103) Dang, L. X.; Chang, T.-M. Molecular Dynamics Study of Water Clusters, Liquid, and Liquid−Vapor Interface of Water with Many-Body Potentials. *J. Chem. Phys.* **1997**, *106*, 8149−8159.
(104) Brown, M. A.; Abbas, Z.; Kleibert, A.; Green, R. G.; Goel, A.; May, S.; Squires, T. M. Determination of Surface Potential and Electrical Double-Layer Structure at the Aqueous Electrolyte-Nanoparticle Interface. *Phys. Rev. X* **2016**, *6*, 011007.
(105) Ma, X.; Li, M.; Pfeiffer, P.; Eisener, J.; Ohl, C.-D.; Sun, C. Ion Adsorption Stabilizes Bulk Nanobubbles. *J. Colloid Interface Sci.* **2022**, *606*, 1380−1394.
(106) Butt, H.-J.; Graf, K.; Kappl, M. *Physics and Chemistry of Interfaces*; John Wiley & Sons, 2023.
(107) Zhang, H.; Guo, Z.; Zhang, X. Surface Enrichment of Ions Leads to the Stability of Bulk Nanobubbles. *Soft Matter* **2020**, *16*, 5470−5477.
(108) Ishiyama, T.; Morita, A. Computational Analysis of Vibrational Sum Frequency Generation Spectroscopy. *Annu. Rev. Phys. Chem.* **2017**, *68*, 355−377.
(109) Liu, J.; Yang, J.; Zeng, X. C.; Xantheas, S. S.; Yagi, K.; He, X. Towards Complete Assignment of the Infrared Spectrum of the Protonated Water Cluster $H^+(H_2O)_{21}$. *Nat. Commun.* **2021**, *12*, 6141.
(110) Crespo, Y.; Hassanali, A. Unveiling the Janus-Like Properties of OH^-. *J. Phys. Chem. Lett.* **2015**, *6*, 272−278.
(111) Litman, Y.; Chiang, K.-Y.; Seki, T.; Nagata, Y.; Bonn, M. Surface Stratification Determines the Interfacial Water Structure of Simple Electrolyte Solutions. *Nat. Chem.* **2024**, *16*, 644−650.

https://doi.org/10.1021/acsphyschemau.3c00076
ACS Phys. Chem Au 2024, 4, 336−346